Journal of Power Sources 454 (2020) 227954

Contents lists available at ScienceDirect

Journal of Power Sources

journal homepage: www.elsevier.com/locate/jpowsour

Electrochemical studies on symmetric solid-state Na-ion full cell using $Na_3V_2(PO_4)_3$ electrodes and polymer composite electrolyte

Sourav Bag [a,b], Chengtian Zhou [a], Samuel Reid [b,**], Shantel Butler [b], Venkataraman Thangadurai [a,*]

[a] Department of Chemistry, University of Calgary, 2500 University Dr NW, Calgary, Alberta, T2N 1N4, Canada
[b] Geometric Energy Corporation, 630 8th Ave SW #600, Calgary, Alberta, T2P 1G6, Canada

HIGHLIGHTS

- Composite polymer electrolyte (CPE) with high Na-ion conductivity is prepared.
- Symmetric solid-state Na-ion full cell is demonstrated with CPE and NASICON electrode.
- Solid-state Na-ion full cell exhibits an energy density of 126 W h kg^{-1}.

GRAPHICAL ABSTRACT

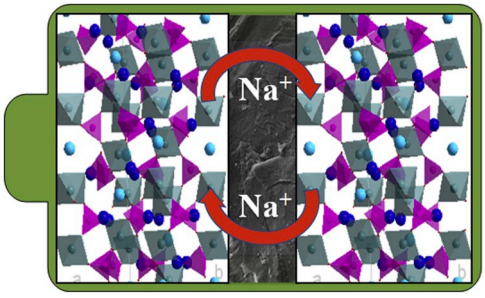

ARTICLE INFO

Keywords:
Composite polymer electrolytes
Solid-state Na-ion battery
$Na_3V_2(PO_4)_3$
Interfaces

ABSTRACT

Ubiquitous low-cost sodium ore is abundant and increasingly of interest for sodium-based battery research for grid-scale energy storage systems. The conventional organic liquid electrolytes in currently used sodium-based batteries endure inflammability, thermal instability, and risk of safety issues. The recent trend in developing solid-state-Li batteries also thrives on exploring the all-solid-state Na battery. Herein, we report a solid-state Na-ion full cell working at room temperature using a polyvinylidene fluoride (PVDF)-based composite polymer electrolyte and $NaZr_2(PO_4)_3$-structured $Na_3V_2(PO_4)_3$ (NVP) electrode. PVDF-based composite polymer electrolyte (CPE) with $NaCF_3SO_3$ salt and SiO_2 filler displays high conductivity with electrochemical stability. The symmetric solid-state full cell delivers a specific capacity of 76 mA h g^{-1} at 0.5C rate, and a specific energy of 126 W h kg^{-1} based on the total mass of the NVP cathode only. The solid-state Na-ion full cell can retain 70% of its initial specific capacity after 100 continuous charge-discharge cycles.

1. Introduction

Lithium-ion batteries (LIBs) are the most promising and successful energy storage devices employedfor electric vehicles, space hardware, portable electronics, mobile commercial assets, and stationary storage applications for their high energy density. However, the scarcity of lithium ores, the increasing demand for electric vehicles (EVs) and portable electronic devices will cause an unsustainable life cycle

* Corresponding author.
** Corresponding author.
E-mail addresses: sam@geometricenergy.ca (S. Reid), vthangad@ucalgary.ca (V. Thangadurai).

https://doi.org/10.1016/j.jpowsour.2020.227954
Received 7 December 2019; Received in revised form 15 February 2020; Accepted 24 February 2020
Available online 9 March 2020

analysis for ongoing LIB production increasing globally. Recent studies from the U.S Geological survey reveal that only 13 million tons of Li are present in the Earth's crust [1,2]. The low abundance of Li ores and their increasing demand and cost are a primary concern for the future of LIB technology towards large-scale stationary energy storage and EV applications. The increasing necessity of energy storage devices and global depletion of lithium ores calls for a new battery chemistry with high energy density for the future. Sodium is the sixth most abundant element in earth's crust, it's inexpensive, and the ease of recyclability makes the sodium-ion battery (SIB) a very promising replacement for LIBs in grid-scale energy storage and EVs. Sodium exhibits similar physical and electrochemical properties to Li [3]. Furthermore, instead of expensive conventional Cu current collector for the negative electrode, inexpensive Al can be employed in SIBs [4,5]. Though a few decades ago, sodium batteries (Na–S battery, ZEBRA battery) have been successfully commercialized for grid scale energy storage and space application, they are operational at high temperature (>250 °C) [6]. High operational temperature and safety issues are still a drawback for Na–S and ZEBRA batteries [7]. The higher ionic radius of Na-ion (1.02 Å) than the Li-ion (0.76 Å) is the main obstacle for ionic diffusion which manifests as poor storage and cycling performance for SIBs [5,8]. Attempts have been made to develop novel electrodes and electrolytes for advanced SIBs [9].

Electrolytes are a fundamental battery component and are key to their overall performance. Currently used liquid organic electrolytes in LIBs and SIBs are flammable, exhibit low thermal stability, and pose safety issues. Solid electrolytes are non-flammable and exhibit high thermal stability and prevent dendrite formation [7]. Furthermore, having a higher ion transference number, solid electrolyte exhibits better kinetic properties than liquid electrolytes [10]. Solid electrolytes are more promising for next-generation batteries due to their enhanced electrochemical stability and better cycle life. Ceramic-based solid electrolytes, which have a very high Na-ion conductivity attracted great attention due to their high mechanical, thermal and electrochemical stability, and effective dendrite suppression [2]. High interfacial resistance with the electrode materials is the major bottleneck of its practical applications [11]. On the other hand, the polymer-based electrolyte has low interfacial resistance with electrode materials and, excellent elastic and electrochemical properties making it very useful for battery application.

Polyethylene oxide (PEO)-based polymers have been extensively studied as solid electrolyte for LIBs and SIBs [12,13]. PEO-based polymers exhibit a high conductivity above 70 °C [14]. The poor Na-ion conductivity of the PEO-based electrolytes at room temperature is the major bottleneck for its practical use in room temperature operation [7,15,16]. Na-ion conduction can be enhanced by introducing some ceramic particles to the polymer matrix [17,18]. These ceramic particles inserted into the polymer matrix impede the crystallization of polymer and improve the Na-ion conduction even at a lower temperature [19]. The types of the ceramic particles, with their corresponding particle size and concentration in the polymer matrix control the ionic conductivity of the polymer-composite electrolyte [20,21]. Though several strategies have been applied to fabricate all-solid-state Na batteries (ASSNBs) using composite polymer electrolyte, still Na-based polymer electrolytes display poor performances at room temperature [16,17,22–29]. ASSNBs using a polymer-based electrolyte reported in literature are working in the temperature range of 60–80 °C [22–29]. To the best of our knowledge, room temperature operating ASSNB with polymer electrolytes have not been reported so far. Moreover, the melting point of metallic Na is 98 °C, and it is close to the operational temperature (60–80 °C) of the polymer electrolytes. As PEO-based solid polymer electrolytes also have a melting point of ~67 °C, it would be a high-risk to operate Na batteries above 80 °C. However, high energy density and efficient ASSNBs operating at room temperature are very crucial for the future energy storage systems. Only a handful of research articles have been published on Na-based solid polymer electrolytes for ASSNBs [22–29].

Herein, we have prepared a composite polymer electrolyte using polyvinylidene fluoride (PVDF) and SiO_2 ceramic particles for ASSNBs. The ionic conductivity of composite solid electrolyte PVDF-$NaCF_3SO_3$–SiO_2 was calculated to be 0.06 mS cm^{-1} at 25 °C. $NaCF_3SO_3$ was dissolved in DMF and SiO_2 particles were dispersed in the PVDF matrix. The composite electrolyte shows a stable electrochemical performance with NASICON structured $Na_3V_2(PO_4)_3$ (NVP) electrode. A high specific capacity of 110 mA h g^{-1} was obtained for the NVP electrode with good cycling performance. A high energy density of 363 Wh kg^{-1} was obtained for the ASSNB (NVP/CPE/Na). A symmetric Na-ion full cell was fabricated using NVP electrodes and CPE which delivered a specific capacity of 76 mA h g^{-1} with an energy density of 126 Wh kg^{-1} based on cathode mass. The Na-ion full cell also retain a specific capacity retention of 70% after 100 consecutive charge-discharge cycles.

2. Experimental section

2.1. Synthesis of PVDF-SiO_2 composite polymer electrolyte (CPE)

PVDF polymer (Alfa Aesar) and Na-trifluoromethanesulfonate ($NaCF_3SO_3$) (Alfa Aesar) with a molar ratio of 9:1 [(–CH_2CF_2)–:Na^+] were dissolved in dimethyl formamide (DMF) (obtained from Sigma-Aldrich) and was continuously stirred to completely dissolve the polymer and Na-salt. SiO_2 powder (obtained from Sigma-Aldrich) with 2 wt. % (with respect to the PVDF weight) was added to the polymer-salt mixture and was ball-milled for 20 min at 200 rpm to prepare a homogeneous slurry. The polymer-ceramic composite slurry was then cast onto a glass plate and dried for 24 h in vacuum oven. A film of PVDF-$NaCF_3SO_3$–SiO_2 CPE was obtained after drying, and the circular disc was cut for further electrochemical and physicochemical measurements. CPEs with different weight percentages of SiO_2 were prepared to optimize the conductivity. Other non-active oxide-based fillers such as Al_2O_3 and ZrO_2 were also added, and concerned electrochemical performances were measured.

2.2. Synthesis of $Na_3V_2(PO_4)_3$

The NVP cathode was prepared by the sol-gel method using CH_3COONa, NH_4VO_3, $NH_4H_2PO_4$, and citric acid (Sigma-Aldrich). In a 0.25 M aqueous solution of citric acid, 8 mM of NH_4VO_3 was added and continued for stirring at 80 °C. After 5 min, the NH_4VO_3 dissolved into solution and turned to a transparent yellow colour. Then the stoichiometric amount of CH_3COONa and $NH_4H_2PO_4$ was added consecutively and continued for stirring at 80 °C. After 2–3 h the solution become gel and it was kept inside a vacuum oven for overnight at 80 °C. After drying in the vacuum oven, a blue coloured powder was obtained, which was then ground and calcined in an inert atmosphere at 350 °C for 4 h and then 800 °C for 8 h. The ramp of heating was 5 °C/min.

2.3. Material characterization

X-ray diffraction (XRD) was carried out using a Bruker D8 Advance diffractometer (Cu-Kalpha ; 40 kV; 40 mA). Field emission scanning electron microscopic (FESEM) analysis was acquired with Carl Zeiss supra 40. Energy dispersive X-ray microanalyzer (OXFORD ISI 300 EDAX) attached to the Carl Zeiss supra 40 FESEM was employed to understand the elemental composition analysis of the electrolyte. Fourier transform infrared (FTIR) spectroscopy from Thermo-Nicolet Nexus 470 instrument was employed to understand the functional group present in the CPE. Raman spectral measurement data was acquired using a Bruker RAM II with a 1064 nm wavelength laser. Thermogravimetric analysis (TGA) was measured using METTLER TOLEDO thermal system TGA/DSC1 (HT 1600). The Gemini VII 2390 surface area analyzer was employed for the measurement of N_2 adsorption-desorption, surface area, and pore size distribution of the NVP powder at 77.3 K. The stress-strain analysis or the mechanical stability of the electrode material was measured using MARK-10 ESM303 Motorized

Tension/Compression Test Stand with capacity of 1.5 kN and strained at 10 mm/min in ambient room temperature. The length and width of the polymer sample was 50 and 9 mm, respectively, with a thickness of 150 μm.

2.4. Electrochemical measurements

The Na-ion conductivity of all the CPEs was measured using AC impedance analysis using the Princeton (Versa STAT 3) instrument with a frequency range of 10 kHz to 0.1 Hz. The CPEs were sandwiched in between two stainless-steel blocking type electrodes. A Teflon made stiff circular spacer was employed to avoid the change in thickness of the compressible polymer. MTI split cell was utilized to measure the ionic conductivity. The ionic conductivity (σ) was estimated using the following equation:

$$\sigma = {}^{l}/_{(A \times R)} \quad (1)$$

where l is the thickness of the electrolyte, A stands for the area of the electrolyte, and R is the obtained resistance. Linear sweep voltammetry (LSV) was carried out to examine the electrochemical stability of the CPE using a CR2032 coin cell. To evaluate the compatibility and stability of the CPE with the Na anode, Na stripping-plating experiments were carried out by sandwiching the CPE in between two Na electrodes as a symmetric Na/CPE/Na cell using a CR2032-coin cell. A suitable Teflon spacer was kept between two Na metal electrodes to maintain a constant thickness of electrolyte. A small amount (5 μL cm^{-2}) of liquid electrolyte was added at the interface of the Na electrode and CPE to reduce the interfacial resistance. Both the interfaces were wetted with the liquid electrolyte. The liquid electrolyte used in this experiment is 1 M $NaClO_4$ (Alfa Aesar) solution in PC (Sigma Aldrich), with 5 wt. % Fluoroethyelene carbonate (Alfa Aesar).

2.5. Electrode modification and cell assembly

As synthesized $Na_3V_2(PO_4)_3$ electrode powder was mixed with super P conductive carbon, PVDF binder, and $NaCF_3SO_3$ with a weight ratio of 7:1.7:1:0.3 in N-methyl pyrrolidone (NMP) solvent and uniformly coated over an Al foil. PVDF and $NaCF_3SO_3$ salt in the electrode matrix not only act as a binder but also provide the path for Na-ion transport. The electrode material coated Al foil was dried in a vacuum oven at 60 °C overnight. The average mass loading of active material was ~1.5 (±0.2) mg cm^{-2}. The cathode coated Al foil was then cut into a 11.6 mm diameter circular disc electrode with area of ~1 cm^2. Metallic Na was cast on one side of the stainless-steel spacer. A CR2032 coin cell was simply fabricated using the cathode disc, CPE, and Na metal anode with addition of 5 μL of liquid electrolyte on both the cathode and anode surface. The liquid electrolyte was carefully added so that the whole electrode area was covered to reduce the interfacial impedance. The circular CPE disc with a diameter of 19 mm and ~60 (±20) μm thickness was sandwiched between the Na discs and cathode coated Al foil. The electrochemical performance of the fabricated Na-cell was evaluated by an MTI Inc., USA battery test station.

2.6. Symmetric full cell fabrication with $Na_3V_2(PO_4)_3$ electrodes

A symmetric Na-ion full cell was fabricated using two NVP electrodes and Na-ion conducting CPE. The dimension of the circular NVP cathode and CPE was the same as the half cell. The calculation of the NVP electrode mass loading for the full cell fabrication is also shown (Fig. S1). The cathode and anode contain active NVP material loading with a weight ratio of 1:2. The anodic disc electrode area was kept higher than the cathode to fully cover and utilize the active material at the cathode. A CR 2032 type coin cell was used, and 5 μL cm^{-2} of liquid electrolyte was employed on both electrode for complete wetting to reduce the interfacial resistance. The liquid electrolyte used in this experiment is 1 M $NaClO_4$ solution in PC with 5 wt.% fluoroethyelene carbonate.

3. Results and discussion

3.1. Characterization of the composite polymer electrolyte (CPE)

Scheme 1 represents the synthetic protocol for the CPE. The PVDF polymer and Na-salt were dissolved in DMF, resulting in a clear viscous solution. Subsequently, SiO_2 was added and ball-milled for 20 min at 200 rpm such that the SiO_2 particles disintegrated and homogeneously disperse in the polymer matrix. The amount of the solvent plays a crucial role in controlling the thickness of CPE film. The microscopic view of the CPE surface shows a solid and rough structure without having any pores on the surface (Fig. 1a and b). The morphology of the CPE is primarily tailored by the Na-salt and type of the filler impregnated in the CPE matrix [30–32]. The digital image of the CPE film shows its flexible nature (Fig. 1c). The cross-sectional microscopic image of the CPE shows the rough and densely packed structure, and exhibits a high conductivity of 0.06 mS cm^{-1} (Fig. 1d and e). The Na-salt and SiO_2 particle filler were not observed in the microscopic image, however, it suggests good miscibility in the polymer matrix. The miscibility of the SiO_2 filler and Na salt were further supported from the area mapping of the CPE (Fig. S2). The dense and continuous single-phase of the polymer matrix has significant advantages in blocking Na dendritic growth and ionic conductivity.

The powder X-ray diffraction (PXRD) pattern reveals the crystalline quartz form of SiO_2 (Fig. 2a). PXRD pattern for the PVDF film displays two intense peaks at 2θ value 20.16° and 18.58°, which are assigned to *110* and *020* planes, respectively. Another peak at 39.46° confirms the gamma (γ) phase of the PVDF [33–35]. Addition of $NaCF_3SO_3$ salt in the PVDF changes the crystalline nature, but the phase (γ) of the PVDF remain the same. No appearance of peaks for $NaCF_3SO_3$ in the PVDF-$NaCF_3SO_3$ complex supports that the salt is completely dissolved in the PVDF. The PXRD pattern for the CPE shows less crystalline nature and shows only three peaks for SiO_2.

The FTIR spectral measurement of the PVDF powder shows characteristic vibrational peaks at 613, 763, 796, 840, 883, 950, 975, 1068, 1188, 1245, 1284, and 1401 cm^{-1} which are well within agreement with the α-phase of PVDF (Fig. 2b) [34,35]. The PVDF film has shown significant characteristic peaks at 808, 834, 873, 1070, 1166, 1234, and 1401 cm^{-1} (Table S1) [34]. All these peaks are ascribed to the γ-phase of the PVDF film. PVDF-$NaCF_3SO_3$ and the CPE exhibits peaks associated with the γ-phase of the PVDF. The β and γ-phase of PVDF more of a polar nature than the alpha phase. The polar nature of the polymer reduces its crystalline properties and enhances ionic conductivity. As a result, the β and γ phases have more electroactive properties compare to the α phase [36,37]. The phase of PVDF film has an influence on the ionic conductivity and electrochemical performance of CPE. The FTIR spectral profile of $NaCF_3SO_3$ displays characteristics symmetric and antisymmetric stretching and bending frequencies for $–CF_3$ and $–SO_3$ (Table S1) [38–40]. All the peaks associated with $NaCF_3SO_3$ and γ-PVDF can be found in both CPE and PVDF-$NaCF_3SO_3$. An additional peak at 1670 cm^{-1} is found for CPE and PVDF-$NaCF_3SO_3$, which is attributed to the amide group of the DMF solvent trapped in the polymer matrix.

The Raman spectral profile of the PVDF powder shows significant characteristics peaks for α-PVDF at 609 and 797 cm^{-1}, which are attributed to CF_2 wagging and stretching, respectively (Fig. 2c). The Raman spectral profile further confirms that the phase of PVDF film has been changed from α to γ (Table S1). Two exclusive peaks at 808 and 839 cm^{-1} correspond to the γ-phase of PVDF [34,35,41]. Raman spectra of $NaCF_3SO_3$ shows three significant characteristics peaks (Table S1) [42,43]. The Raman spectral profile for CPE shows the similar spectral behaviour of γ-PVDF and $NaCF_3SO_3$.

To further understanding of the CPE composition, thermogravimetric analysis (TGA) was carried out in air for CPE, PVDF-$NaCF_3SO_3$,

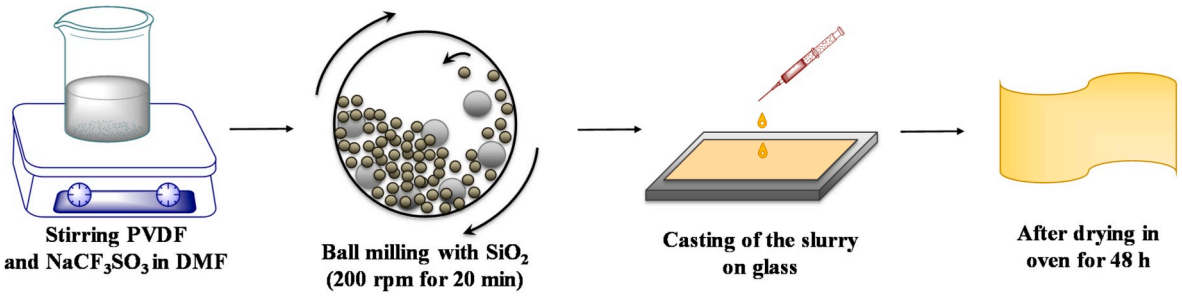

Scheme 1. Schematic illustration of the synthesis of the composite polymer electrolyte (CPE) membrane.

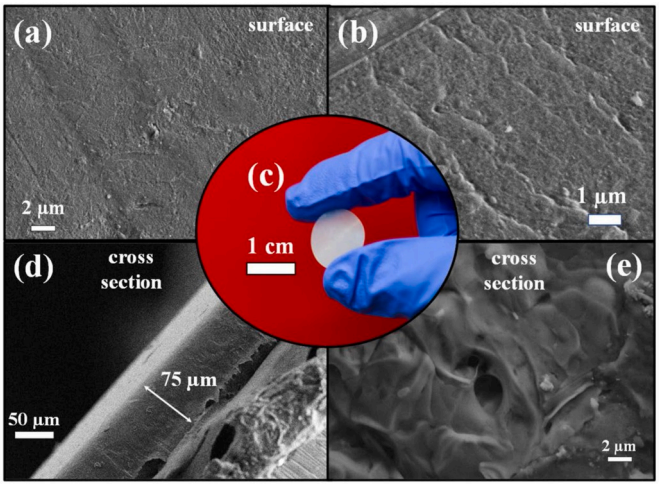

Fig. 1. (a, b) FESEM image of CPE surface, (c) digital image of circular CPE film, and (d, e) cross-sectional SEM image of the CPE membrane.

PVDF, and SiO_2 (Fig. 2d). The thermogram of SiO_2 does not show any significant mass change up to 800 °C. The TGA profile for PVDF powder shows an onset of mass loss after 388 °C. The PVDF-$NaCF_3SO_3$ and CPE show distinct thermogram when compared to the PVDF powder. A continuous mass loss for CPE and PVDF-$NaCF_3SO_3$ was observed up to 180 °C. This mass loss is associated with the evaporation of the trapped DMF solvent inside the PVDF matrix. The amount of the DMF solvent trapped inside the PVDF is about 8 wt. %. We believe the trapped DMF inside the polymer acts as a plasticizer and improves the ionic conductivity of the CPE. Though the addition of plasticizer has a detrimental effect on mechanical stability and dendrite blocking, our electrochemical experiments further support that 8% DMF inside the CPE does not affect the mechanical strength of the solid electrolyte. For the evaluation of mechanical stability of the CPE, the stress-strain curve is analysed (Figure S2d, see supporting information). The CPE film displays an ultimate tensile stress of 16 MPa and strain of 135%.

3.2. *Characterization of the NASICON structured $Na_3V_2(PO_4)_3$ electrode*

The X-ray diffraction pattern of the electrode material confirms the synthesis of NASICON structured NVP (Fig. S3a) [44]. NVP shows that the VO_6 octahedra shares all of its corners with PO_4 tetrahedra. One Na^+

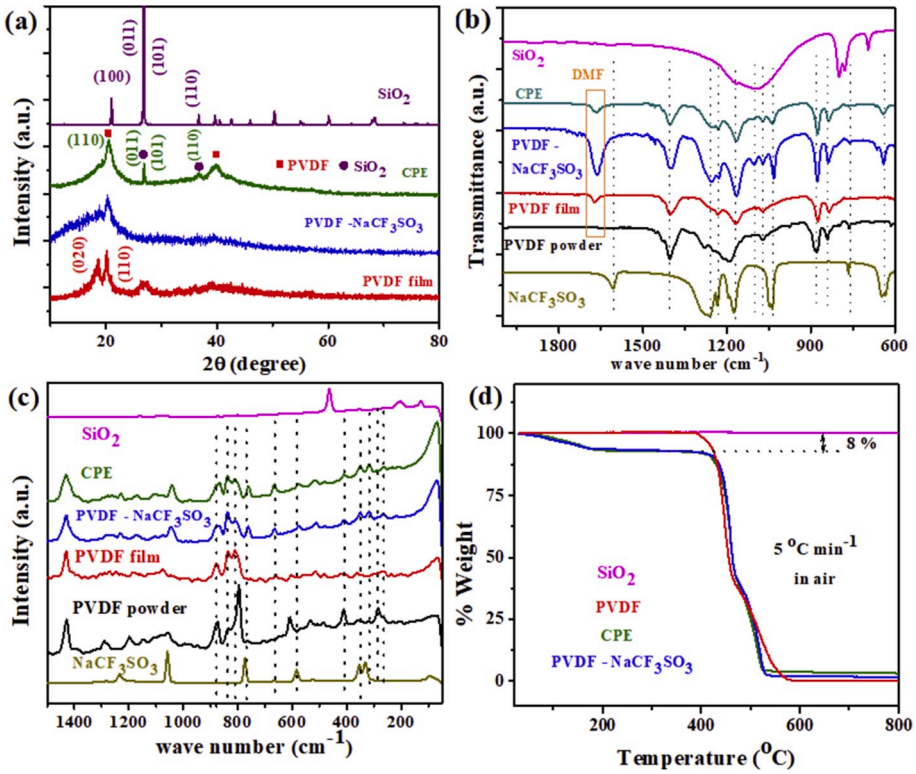

Fig. 2. (a) X-ray diffraction (XRD) pattern, (b) FTIR, (c) Raman spectral profile, and (d) Thermogravimetric analysis (TGA) of SiO_2, PVDF, PVDF-$NaCF_3SO_3$ and CPE.

ion occupy the six-fold coordinated site (M1) whereas two Na^+ occupies the eight-fold coordinated site (M2). The two Na^+ at the eight-fold coordinated site (M2) is weakly bound to the surrounded oxygen atoms and can be extracted at a potential range of 3.4 V/Na whereas another Na^+ can be inserted at the six-fold coordinated site (M1) while discharging below 1.6 V/Na (Fig. S3b) [45]. The thermogravimetric analysis shows that the NVP cathode contains 1.7 wt.% of carbon (Fig. S3c). The porous microstructure of the electrode material was found from the SEM image (Figs. S3d–e). The average particle size of the NVP particles is 2 μm (Figure S3f, see supporting information). The EDAX profile and elemental analysis further support successful formation of the NVP (Fig. S3g). The surface area of the NVP electrode was measured using Brunauer-Emmett-Teller (BET) method and found to be 25.7 $m^2 g^{-1}$. The average pore size was analysed using Barrett–Joyner–Halenda (BJH) method and found to be 12 nm (Figure S3h, see supporting information). Despite a high theoretical capacity (272 mA h g^{-1}) of $LiCoO_2$ it can only deliver a reversible practical specific capacity of 140 mA h g^{-1}. $LiCoO_2$ also shows very fast capacity decay and safety issues because of the surface oxygen loss. $LiFePO_4$ is a very promising cathode material for Li-ion batteries but its low Li^+ diffusion constant forbids its operation at a high current rate. Nanosized $LiFePO_4$ and carbon coating improves the performance of the $LiFePO_4$ electrode [46]. The NVP electrode consist of three-dimensional framework of [PO_4] tetrahedra and [VO_6] octahedra with strong covalent bonding of oxygen in the polyanion polyhedral owing to better thermal stability, long cycle life and excellent safety feature. Furthermore, the 3D crystal structure shows fast Na^+ kinetics which improves the electrochemical performances [47].

3.3. Electrochemical performance of CPE

CPE attains an ionic conductivity value of 6.0×10^{-5} Scm^{-1} at 25 °C. The ratio of PVDF, $NaCF_3SO_3$, and SiO_2 was optimized to achieve a high CPE conductivity (Fig. S4). The electrochemical impedance spectral (EIS) profile for the CPE at different temperatures is shown in Fig. S5a. The ionic conductivity of CPE and PVDF-$NaCF_3SO_3$ shows Arrhenius behavior. An increase in temperature facilitates the expansion of polymeric chain, which produces free volume inside the polymer. The as-produced free-volume enhances the segmental motion of the polymer, which increases the ionic conductivity [19,41]. The Arrhenius plot for CPE and PVDF-$NaCF_3SO_3$ solid electrolytes is shown in Fig. 3a. A conductivity of 2.1×10^{-6} S cm^{-1} was measured at 25 °C for PVDF-$NaCF_3SO_3$. The addition of SiO_2 to PVDF-$NaCF_3SO_3$ reduces the crystalline nature of the PVDF, which eventually enhances the ionic conductivity in CPE. The ceramic fillers not only enhance the amorphous nature of the polymer but also augment the conductivity by proper orientation of the dipoles which play a crucial role in determining ionic conductivity [48,49]. It is important to mention that the CPE and PVDF-$NaCF_3SO_3$ contain 8 wt.% of DMF solvent found (Fig. 2b and d). The trapped DMF solvent inside the PVDF act as a plasticizers and enhance the overall conductivity [49,50].

SiO_2 of different size and amount in the polymer matrix change the structure and crystallinity of the polymer. Potential hydroxyl (-OH) moieties on the surface of SiO_2 seem to facilitate in the formation of hydrogen bonding (O–H⋯F–C) with the –CF_2 group present in the PVDF polymer (Fig. S6). Due to the presence of the highly polar –OH group on the SiO_2 surface, the SiO_2 particle acts as a nucleating agent of the PVDF phase. The lower size and higher surface area of SiO_2 enhance the –OH concentration and increase the associated hydrogen bond (O–H⋯F–C), which eventually controls the phase of the PVDF polymers. Higher amount of SiO_2 particles inside the polymer matrix also have influence on polymer phase formation but the possibilities of particle agglomeration may decrease the overall SiO_2 surface area and disruption of effective phase control for the polymer. Moreover, the surface of the SiO_2 can accommodate the solvent (e.g., DMF) which will act as a plasticizer and have an influence on the polymer phase. Therefore, the type and size of SiO_2 particles play a crucial role to determine the crystallinity and structure of the polymer [51,52].

The activation energy for ionic conduction of the PVDF-$NaCF_3SO_3$ and CPE is calculated to be 0.33 and 0.28 eV, respectively. The CPE exhibits a lower activation energy (E_a) than the PVDF-$NaCF_3SO_3$ because of the facile Na-ion hopping through the amorphous region of the PVDF due to the presence of SiO_2. However, the conductivity of the investigated CPE is low and could only achieve decent conductivity at above 60 °C. Most of the ASSNBs are reported so far as operating above 60 °C [17,22–29]. To best of our knowledge, so far, high conductivity (>10^{-4} S cm^{-1}) for a Na-based dry solid polymer electrolyte at room temperature is not achieved.

To evaluate the chemical and electrochemical stability of CPE against Na metal galvanostatic cycling with a constant areal current density of 0.2 mA cm^{-2} was carried out using a symmetric Na/CPE/Na cell (Fig. 3b). We have tried to accomplish the galvanostatic experiments with a pure solid interface, but we found substantial interfacial resistance from the EIS spectra (Figure S7, see supporting information). So, we have introduced 5 μL cm^{-2} of liquid electrolyte on both the Na electrodes to minimize the interfacial resistance that improved the overall conductivity. The calculated electrolyte uptake (~80%) of the CPE is significantly higher than the amount of added liquid electrolyte. The polarity of current for the galvanostatic experiment was switched every 30 min. The galvanostatic cycling profile for the CPE affirms its excellent stability for more than 1000 h (Fig. 3b). The stable galvanostatic profile further supports the mechanical stability of the CPE and dendrite blocking. The galvanostatic profiles at different times are shown in Figure S8, see supporting information. The higher voltage during the beginning of galvanostatic cycles is associated with overpotential developed due to Na-ion reduction and oxidation associated with the galvanostatic cycling process and Na-ion transport through the electrode/electrolyte interphase or solid electrolyte interphases [53]. We have also evaluated the possibilities of using different fillers (Al_2O_3

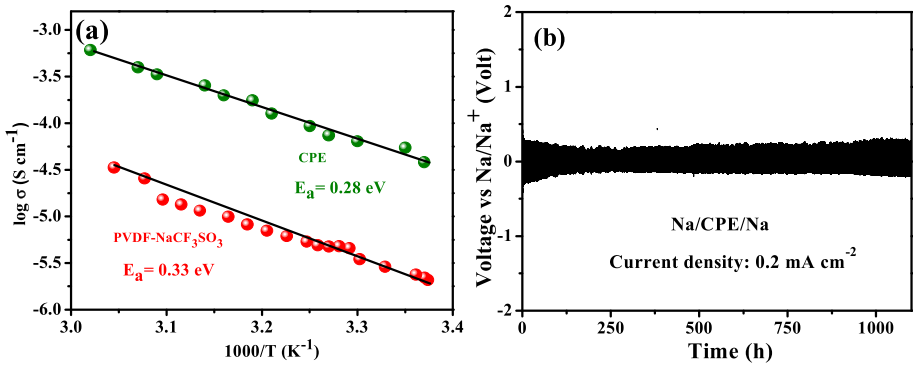

Fig. 3. (a) Arrhenius plot for the PVDF-$NaCF_3SO_3$ and CPE, and (b) galvanostatic profile of CPE at a constant current density of 0.2 mA cm^{-2} with the symmetric cell (Na/CPE/Na) configuration.

and ZrO_2) to formulate an efficient CPE. But the higher conductivity and relatively superior galvanostatic profile for CPE-SiO_2 than other ceramic-doped CPEs (Al_2O_3 and/or ZrO_2 doped) make it suitable for battery applications (Figure S9, see supporting information.). The electrochemical stability window of the CPE was evaluated by a linear sweep voltammetry experiment (Figure S5b, see supporting information). It was found that the CPE is stable up to 4.1 V/Na as no decomposition peaks were as observed before 4.1 V/Na. The pair of redox peaks observed at ~0 V is attributed to the Na^+ stripping and plating.

3.4. Electrochemical performance of the $Na_3V_2(PO_4)_3$ electrode with the CPE

To evaluate the practical application of the CPE, electrochemical performances of the NVP were studied with the CPE against Na metal (Scheme 2a). The cyclic voltammogram of the NVP within the voltage range of 1–4 V against Na/Na^+ (1–4 V/Na) metal shows two redox couple peaks (Fig. S10). The redox peak at the higher potential (3.3–3.4 V/Na) is attributed to the (V^{4+}/V^{3+}) redox couple and/or oxidation of $Na_3V_2(PO_4)_3$ to $NaV_2(PO_4)_3$ due to Na^+ intercalation and de-intercalation, i.e. [54–56],

$$Na_3V_2(PO_4)_3 \rightleftharpoons 2Na^+ + 2e^- + NaV_2(PO_4)_3 \quad (2)$$

The other redox peak at the lower potential (~1.6 V/Na) is ascribed to the (V^{3+}/V^{2+}) redox couple in NVP electrode, i.e.,

$$Na_3V_2(PO_4)_3 + Na^+ + e^- \rightleftharpoons Na_4V_2(PO_4)_3 \quad (3)$$

This voltammogram indicates excellent compatibility of the NVP electrode with the CPE. However, the cathodic peak current (i^P_a) at 1.38 V/Na for the first cathodic scan was obtained, and reduced in the consecutive scans. The high current for the first cathodic scan may be attributed to the solid electrolyte interphase (SEI) formation [57–59]. On the other hand, a small anodic shoulder peak at ~2.2 V/Na was observed only for the first cycle, which gradually disappeared in consecutive cycles. The shoulder peak may be attributed to either the poor Na^+ diffusion kinetics of the M1 site of the NVP electrodes or the poor ionic conductivity of the CPE [56]. The voltammogram further suggests CPE would be successful in the fabrication of a symmetric solid-state Na-ion full cell with the NVP electrodes. The peak to peak separation (ΔE_p) for the (V^{3+}/V^{2+}) and (V^{4+}/V^{3+}) was obtained to be 0.5 and 0.6 V, respectively, which are higher than the voltammogram measured with the liquid electrolyte [55]. The higher ΔE_p value could be due to the low ionic conductivity of the CPE. The two distinct peaks for NVP at the potential of 3.4 V/Na and 1.6 V/Na clearly demonstrates the bipolar nature of the electrode material. The theoretical gravimetric cathode capacity associated with 2 Na^+ intercalation at 3.4 V/Na is 117.6 mA h g^{-1} whereas the theoretical anode capacity of NVP is 58.8 mA h g^{-1} which corresponds to 1 Na^+ at a potential of 1.6 V/Na [60].

The electrochemical properties of the NVP cathode were further evaluated using the CPE electrolyte and the metallic Na anode. The charge-discharge profile of the NVP electrode as a cathode material within a voltage range of 2–4 V/Na at 0.5 C rate is shown in Fig. 4a. The charge profile demonstrates a plateau at a voltage of 3.5 V/Na, which is associated with the oxidation of NVP and displays a maximum specific capacity of 120 mA h g^{-1}. Similarly, a discharge capacity of 102 mA h g^{-1} for the first cycle was also obtained with a discharge plateau at 3.27 V (Fig. 4b). A hysteresis loss is observed in the charge-discharge profile due to the low conductivity of the CPE. But the NVP electrode shows an outstanding cycling performance with 86% capacity retention after 250 consecutive charge-discharge cycles at 0.5 C rate. Coulombic efficiency of the cell shows an average value of more than 98%, which suggests a stable performance of the CPE with the NVP electrode. However, for the first 40 cycles, the Coulombic efficiency was not high due to unstable SEI formation on the Na surface. The liquid electrolyte employed in the cell seems to be consumed to build an effective SEI on the Na surface [58]. During the galvanostatic experiments with symmetric Na/CPE/Na cell and from EIS spectra, we obtained a very high interfacial resistance (Figure S7, see supporting information). We propose the high interfacial resistance is because an effective interfacial layer was lacking at the CPE-Na solid interface. In our previous study, an effective interfacial layer formation was shown on the PVDF-based solid electrolyte at the Li surface [41]. The interfacial layer formed at the PVDF interface was crucial for the Li-ion transfer from the electrolyte to electrode and vice versa while blocking the electron. Similarly, an efficient and stable interfacial layer formation on CPE or Na metal is also very crucial for the cell operation and inhibits Na dendrite formation. Herein, the used liquid electrolyte is allowing the generation of an effective interfacial layer or solid electrolyte interphase (SEI) on the Na surface. Most of the all-solid-state-battery (ASSB) with PEO-based solid/composite polymer electrolytes are operational above 60 °C, which is near to the melting point of PEO (67 °C). At high temperature, the polymer electrolytes probably reach liquid state, and a stable SEI is formed, which facilitates the ASSB operation [61].

Song et al. demonstrated poor ASSNBs performance with PEO-based CPE (incorporated with ionic liquid) even with a high ionic conductivity of 1.3×10^{-3} S cm^{-1} at room temperature [23]. The cell was operational above 60 °C at a 0.5 C rate and significant capacity fading was also observed [23]. The rate performance of the electrochemical cell is an important parameter to evaluate the overall quality of the cell. The rate performance of NVP/CPE/Na cell was carried out with different discharge rates and shown in Fig. 4c The NVP electrode shows a specific discharge capacity of 111, 102, 83, and 54 mA h g^{-1} at a C-rate of 0.5, 1, 2, and 5 C. At a discharge rate of 0.5 C, a specific capacity of 109 mA h g^{-1} was recovered. The dQ/dV vs V plot for the 2nd and 100th charge-discharge cycles of NVP cathode shows two peaks, which are attributed to the V^{3+}/V^{4+} redox couple (Fig. S11). The values of potential polarization (ΔE) for the 2nd and 100th charge-discharge cycles are 0.265 V and 0.29 V, respectively. The high value for potential polarization (ΔE) is due to the sluggish Na^+ kinetics and poor ionic conductivity of solid electrolyte. However, the observed peak broadening

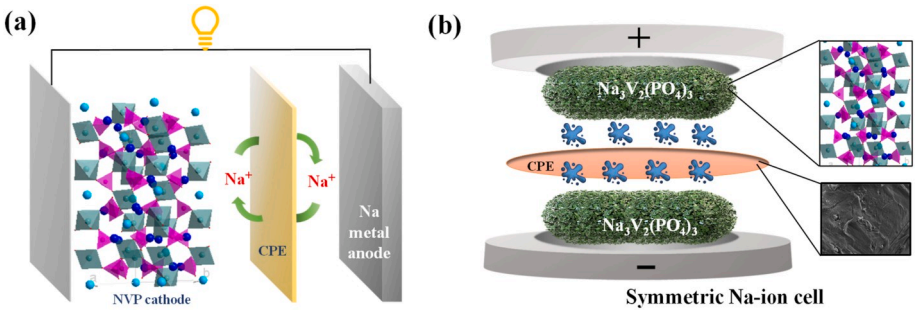

Scheme 2. Schematic illustration of (a) NVP/CPE/Na half cell, and (b) symmetric Na-ion full cell with NVP electrodes and composite polymer electrolyte (CPE) membrane.

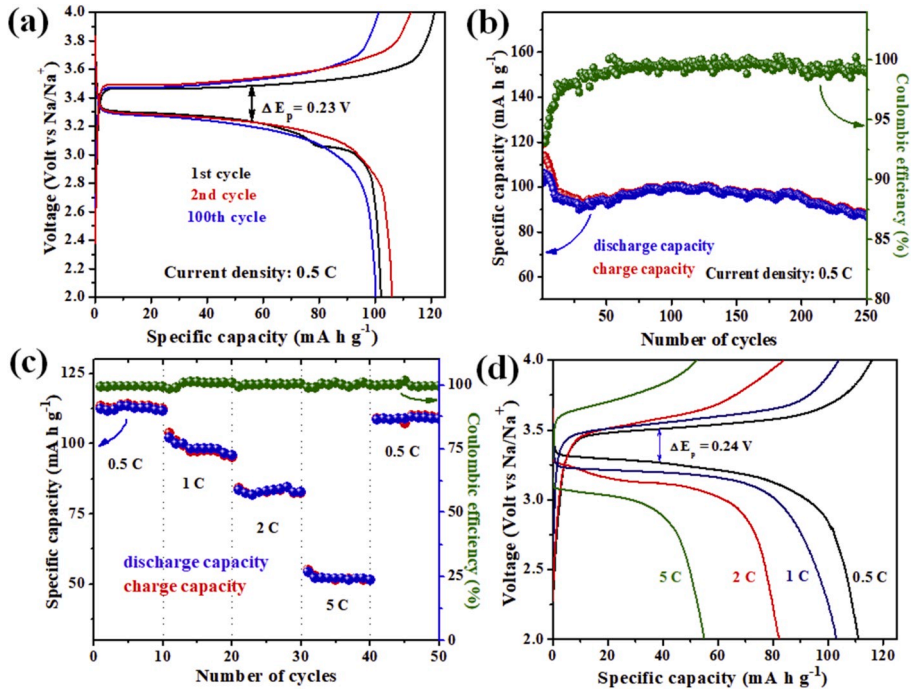

Fig. 4. (a) Charge-discharge profile of the NVP electrode (NVP/CPE/Na) within 2–4 V and corresponding, (b) cycling performance of the half cell at 0.5 C rate, (c) rate performance of NVP electrode, and (d) corresponding charge-discharge profile at different C rate.

from 2nd to 100th cycle is ascribed to the structural changes due to large Na^+ ion insertion/de-insertion [62,63].

The electrochemical performance of the NVP as an anode material was also evaluated. A continuous charge-discharge cycling of the NVP anode was carried out within the potential range of 1–2.5 V/Na at the 0.5 C rate (Fig. S12a). A specific capacity of 57 mA h g^{-1} was obtained at the 0.5 C rate. The discharge profile shows a plateau at 1.5 V attributed to equation (2). The NVP electrode shows decent recyclability with a capacity retention of ~67% from the 2nd discharge capacity value after 200 continuous charge-discharge cycles. A constant capacity fading was observed for the first 50 cycles. The capacity fading is attributed to the unwanted side reaction and loss of liquid electrolyte due to the formation of an unstable SEI [57,59]. The loss of liquid electrolyte reduced the overall conductivity of the cell and was reflected in the charge-discharge profile. A significant change in the hysteresis loss from the 2nd to 50th cycle is also observed (Fig. S12b). The irreversible side reactions were also reflected in the Coulombic efficiency as it reaches a value of 97% after 50 charge-discharge cycles. The specific capacity was stable after 50 cycles and Coulombic efficiency shows an average value of more than 97% after 50 cycles. This phenomenon further supports that the side reactions were ceased, and a stable SEI has been formed after 50 cycles. The NVP anode shows a specific capacity of 61, 35, and 17 mA h g^{-1} at a C-rate of 0.5, 1, and 2 C, respectively (Fig. S12c-d). While returning to the 0.5C rate, it can retain a specific capacity of 48 mA h g^{-1}. At a 2 C rate, a capacitive-type response was obtained (Fig. S12d) and is attributed to poor Na^+ diffusion kinetics in NVP electrode. It is already proven that the Na^+ insertion at the M1 site of the NVP electrode is kinetically sluggish [56,64].

3.5. Electrochemical performance of symmetric solid-state Na-ion full cell

A symmetric Na-ion full cell was fabricated using the NVP electrode and the CPE (Scheme 2b). 5 μL of liquid electrolyte was employed on both the side of the CPE. The discharge profile within a voltage range of 1–2.5 V shows a plateau at 1.68 V with a specific capacity of 76 mA h g^{-1} (cathode limited) at 0.5 C rate for the first cycle (Fig. 5a). Corresponding charge-discharge reactions with the associated electrodes can be written as [44,55]:

$$\textit{Positive electrode reaction}: \; Na_3V_2^{(III)}(PO_4)_3 \rightleftharpoons 2Na^+ + 2e^- + NaV_2^{(IV)}(PO_4)_3 \tag{4}$$

$$\textit{Negative electrode reaction}: Na_3V_2^{(III)}(PO_4)_3 + Na^+ + e^- \leftrightharpoons Na_4V_2^{(II,III)}(PO_4)_3 \tag{5}$$

Overall reaction :

$$Na_3V_2^{(III)}(PO_4)_3 + 2Na_3V_2^{(III)}(PO_4)_3 \rightleftharpoons NaV_2^{(IV)}(PO_4)_3 + 2\,Na_4V_2^{(II,III)}(PO_4)_3 \tag{6}$$

During the charging phase, Na^+ are extracted from the NVP cathode/positive electrode to form $NaV_2(PO_4)_3$ and are also Na^+ inserted into the NVP (anode) to form $Na_4V_2(PO_4)_3$. Beside high specific capacity, as fabricated, the Na-ion full cell also shows excellent cyclic performance for 100 cycles at a 0.5 C rate with a capacity retention of ~70% from its first cycle (Fig. 5b). We have found an initial capacity decay from the first cycle to 25th cycle. We have seen that the NVP anode also undergoes similar capacity fading at the initial cycles. The irreversible capacity loss observed at the initial cycles for a full cell is attributed to the poor anode performance. The Coulombic efficiency of the full cell was also found to be above 95% after 10 charge-discharge cycles, which supports the stable performance of the full cell after initial cycles. The cyclic voltammogram of the full cell shows an anodic peak at 1.9 V, which is due to the de-intercalation of Na^+ from the NVP cathode and Na^+ intercalation to the anode (Fig. S13). The cathodic peak was observed in the voltammogram at 1.81 V for the first scan. The Na-ion full cell exhibits a discharge capacity of 74, 68, and 61 mA h g^{-1} at 0.5, 1, and 2 C rate, respectively. While returning to the discharge at the 0.5C rate, it could be able to retain a specific capacity of 65 mA h g^{-1}. The discharge capacity after returning to the 1 and 0.5 C rate is lower than the initial values. We believe that the drop in the discharge capacity of full cell is attributed to the poor performance of NVP anode. In case of NVP anode a gradual capacity decay was also observed for the first 50 cycles. Even the values for discharge and charge capacity for the full cell

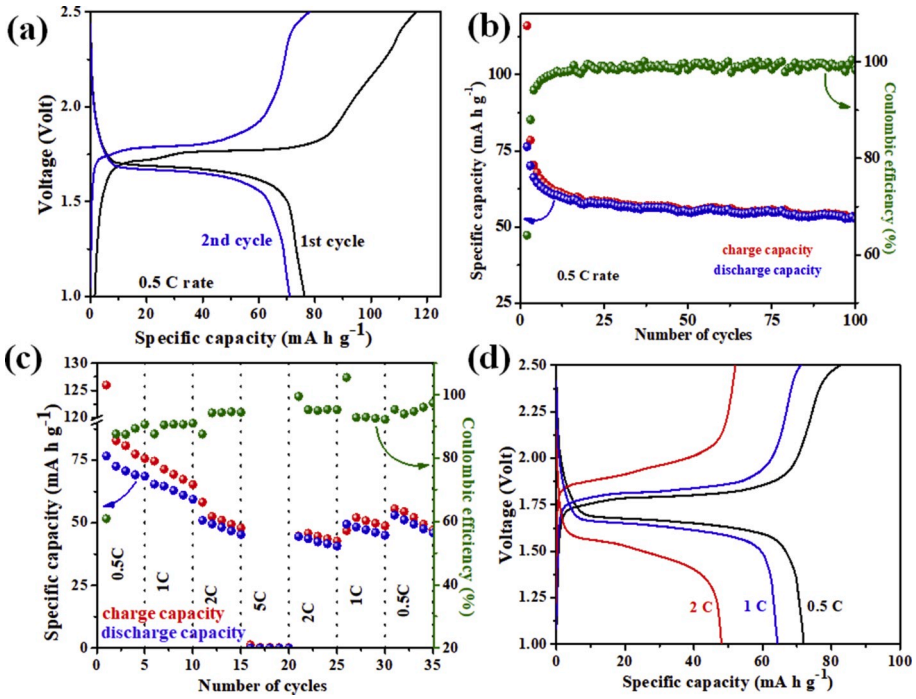

Fig. 5. Electrochemical performance of the symmetric solid-state Na-ion full cell (NVP/CPE/NVP). (a) Charge-discharge profile and corresponding (b) cycling performance at 0.5C rate, (c) Rate performance of the full-cell, and (d) corresponding charge-discharge profile at different C rates.

was different for each current density. This difference may be attributed to the inadequate Na-ion storage due to poor Na-ion kinetics and interfacial layer formation on the anode surface [65]. The poor performance of the cell at high current density is attributed to the poor ionic conductivity of the CPE and poor kinetic performance of the NVP anode. However, our room temperature operating solid-state Na-ion full cell shows high capacity and good cycling performance compared to the reported Na-ion battery with liquid electrolytes (Table S2, see supporting information) [44,55,66,67].

In order to understand the functional mechanism and fate of the CPE and NVP electrode material, post-mortem analysis was carried out after 50 charge-discharge cycles. The post-mortem SEM image of the CPE shows that no significant microstructural changes were found after 50 charge-discharge cycles (Fig. S14a-c). However, the post-mortem XRD pattern of CPE shows that the corresponding characteristic peak for the PVDF and SiO_2 is no longer present, and a new peak appeared at 13.38° (Fig. S14d). This suggests that the crystallinity of the CPE is lost after charge-discharge cycles. For further understanding of the change in the crystallinity of CPE, we have performed XRD measurement of CPE after soaking it in 5 mL of 1 M $NaClO_4$ in PC electrolyte over 100 h. It shows only a small hump for at 13.38° and retains its crystalline nature of PVDF and SiO_2. So, the continuous charge-discharge cycle has a significant role in converting the CPE to an amorphous phase, which enhances the ionic conductance as well as electrochemical performance. The ionic conductivity of the CPE after 50 charge-discharge cycles have been measured and found to be 1.1×10^{-4} Scm^{-1}. However, we have also carried out a TGA measurement after 50 charge-discharge cycles and it shows that the CPE undergoes a higher amount of mass loss (~12%) due to solvent evaporation. The 4% increase in solvent in the CPE after charge-discharge cycles appear from the added liquid electrolyte, which acts as a plasticizer to enhance the conductivity of the electrolyte. The XRD profile further supports the change in the crystallinity of the CPE which is attributed to the presence of liquid electrolyte and continuous charge-discharge cycles. FTIR and Raman spectral profile of the CPE shows no significant changes in the functional group of PVDF and $NaCF_3SO_3$ (Fig. S14e-f). Only three new peaks that appeared in the FTIR spectral profile are attributed to the trapped propylene carbonate (PC). The NVP electrode adhered to the CPE, and the XRD pattern shows all the characteristic peaks for NVP along with the hump at 13.38° for the CPE. The post-mortem XRD pattern and SEM images show the NVP electrode retains its original phase and morphology even after 50 cycles (Fig. S15a-c).

4. Conclusion

In summary, a SiO_2 doped PVDF-$NaCF_3SO_3$ composite polymer electrolyte was developed, which showed an ionic conductivity of 0.06 mS cm^{-1} at 25 °C. CPE exhibits a stable electrochemical performance up to 4.1 V/Na with excellent galvanostatic cycling for more than 1000 h. The NVP electrode shows satisfactory rate capability and a long cycling performance with the CPE. The solid-state Na battery made of CPE with an NVP cathode and Na anode can deliver an energy density of 360 Wh kg^{-1} (based on cathode mass) at 0.5C and can retain 162 W kg^{-1} at 5C rate. Symmetric solid-state Na-ion full cells with NVP electrodes and CPE electrolytes can deliver a high specific capacity of 76 mA h g^{-1} at with an energy density 126 Wh kg^{-1} at 0.5C. A good cycling performance was also observed with a specific capacity retention of 70% from its initial value after 100 cycles. The excellent performance of symmetric and asymmetric solid-state Na batteries at room temperature opens new possibilities for the next generation of environment-friendly electrochemical energy storage systems.

Author contributions

S. Bag and V. Thangadurai conceptualized the research and designed the experimental aspects. S. Bag carried out all the experiments and collected the data. All the authors contributed to data analysis and manuscript writing.

Declaration of competing interest

The authors declare that they have no known competing financial interests or personal relationships that could have appeared to influence the work reported in this paper.

Acknowledgements

We would like to acknowledge the support from Mitacs, a Canadian national research organization, and Geometric Energy Corporation, a Canadian research and development company. Sourav Bag is a recipient of a MITACS Elevate postdoctoral fellowship with Geometric Energy Corporation. Authors acknowledge Dr. Xia Tong, Sina Rezvani, and Prof. Simon Park for their help in experiments and fruitful discussion.

Appendix A. Supplementary data

Supplementary data to this article can be found online at https://doi.org/10.1016/j.jpowsour.2020.227954.

References

[1] Q. Ni, Y. Bai, F. Wu, C. Wu, Polyanion-type electrode materials for sodium-ion batteries, Adv. Sci. 4 (2017), 1600275.
[2] C. Zhou, S. Bag, V. Thangadurai, Engineering materials for progressive all-solid-state Na batteries, ACS Energy Lett 3 (2018) 2181–2198.
[3] D. Kundu, E. Talaie, V. Duffort, L.F. Nazar, The emerging chemistry of sodium ion batteries for electrochemical energy storage, Angew. Chem. Int. Ed. 54 (2015) 3431–3448.
[4] L. Schafzahl, I. Hanzu, M. Wilkening, S.A. Freunberger, An electrolyte for reversible cycling of sodium metal and intercalation compounds, ChemSusChem 10 (2017) 401–408.
[5] C. Vaalma, D. Buchholz, M. Weil, S. Passerini, A cost and resource analysis of sodium-ion batteries, Nat. Rev. Mater. 3 (2018) 18013.
[6] X. Lu, G. Li, J.Y. Kim, D. Mei, J.P. Lemmon, V.L. Sprenkle, J. Liu, Liquid-metal electrode to enable ultra-low temperature sodium–beta alumina batteries for renewable energy storage, Nat. Commun. 5 (2014) 4578.
[7] H. Che, S. Chen, Y. Xie, H. Wang, K. Amine, X.-Z. Liao, Z.-F. Ma, Electrolyte design strategies and research progress for room-temperature sodium-ion batteries, Energy Environ. Sci. 10 (2017) 1075–1101.
[8] J.-Y. Hwang, S.-T. Myung, Y.-K. Sun, Sodium-ion batteries: present and future, Chem. Soc. Rev. 46 (2017) 3529–3614.
[9] K. Kubota, S. Komaba, Review—practical issues and future perspective for Na-ion batteries, J. Electrochem. Soc. 162 (2015) A2538–A2550.
[10] Z. Zhang, Y. Shao, B. Lotsch, Y.-S. Hu, H. Li, J. Janek, L.F. Nazar, C.-W. Nan, J. Maier, M. Armand, L. Chen, New horizons for inorganic solid state ion conductors, Energy Environ. Sci. 11 (2018) 1945–1976.
[11] S. Narayanan, S. Reid, S. Butler, V. Thangadurai, Sintering temperature, excess sodium, and phosphorous dependencies on morphology and ionic conductivity of NASICON $Na_3Zr_2Si_2PO_{12}$, Solid State Ionics 331 (2019) 22–29.
[12] H. Gao, L. Xue, S. Xin, K. Park, J.B. Goodenough, A plastic–crystal electrolyte interphase for all-solid-state sodium batteries, Angew. Chem. Int. Ed. 56 (2017) 5541–5545.
[13] H. Gao, W. Zhou, K. Park, J.B. Goodenough, A sodium-ion battery with a low-cost cross-linked gel-polymer electrolyte, Adv. Energy Mater. 6 (2016), 1600467.
[14] Solid State Electrochemistry, Cambridge University Press, Cambridge, 1994.
[15] J.-K. Kim, Y.J. Lim, H. Kim, G.-B. Cho, Y. Kim, A hybrid solid electrolyte for flexible solid-state sodium batteries, Energy Environ. Sci. 8 (2015) 3589–3596.
[16] Q. Ma, J. Liu, X. Qi, X. Rong, Y. Shao, W. Feng, J. Nie, Y.-S. Hu, H. Li, X. Huang, L. Chen, Z. Zhou, A new Na[(FSO_2)(n-$C_4F_9SO_2$)N]-based polymer electrolyte for solid-state sodium batteries, J. Mater. Chem. A 5 (2017) 7738–7743.
[17] X. Yu, L. Xue, J.B. Goodenough, A. Manthiram, A high-performance all-solid-state sodium battery with a poly(ethylene oxide)–$Na_3Zr_2Si_2PO_{12}$ composite electrolyte, ACS Mater. Lett. 1 (2019) 132–138.
[18] R.A. Vaia, S. Vasudevan, W. Krawiec, L.G. Scanlon, E.P. Giannelis, New polymer electrolyte nanocomposites: melt intercalation of poly(ethylene oxide) in mica-type silicates, Adv. Mater. 7 (1995) 154–156.
[19] S.B. Aziz, T.J. Woo, M.F.Z. Kadir, H.M. Ahmed, A conceptual review on polymer electrolytes and ion transport models, J. Sci.: Adv. Mater. Dev. 3 (2018) 1–17.
[20] F. Capuano, F. Croce, B. Scrosati, Composite polymer electrolytes, J. Electrochem. Soc. 138 (1991) 1918–1922.
[21] W. Liu, S.W. Lee, D. Lin, F. Shi, S. Wang, A.D. Sendek, Y. Cui, Enhancing ionic conductivity in composite polymer electrolytes with well-aligned ceramic nanowires, Nat. Energy 2 (2017) 17035.
[22] Z. Zhang, Q. Zhang, C. Ren, F. Luo, Q. Ma, Y.-S. Hu, Z. Zhou, H. Li, X. Huang, L. Chen, A ceramic/polymer composite solid electrolyte for sodium batteries, J. Mater. Chem. A 4 (2016) 15823–15828.
[23] S. Song, M. Kotobuki, F. Zheng, C. Xu, S.V. Savilov, N. Hu, L. Lu, Y. Wang, W.D. Z. Li, A hybrid polymer/oxide/ionic-liquid solid electrolyte for Na-metal batteries, J. Mater. Chem. A 5 (2017) 6424–6431.
[24] Z. Zhang, K. Xu, X. Rong, Y.-S. Hu, H. Li, X. Huang, L. Chen, $Na_{3.4}Zr_{1.8}Mg_{0.2}Si_2PO_{12}$ filled poly(ethylene oxide)/$Na(CF_3SO_2)_2N$ as flexible composite polymer electrolyte for solid-state sodium batteries, J. Power Sources 372 (2017) 270–275.
[25] Y.L. Ni'mah, M.-Y. Cheng, J.H. Cheng, J. Rick, B.-J. Hwang, Solid-state polymer nanocomposite electrolyte of TiO_2/PEO/$NaClO_4$ for sodium ion batteries, J. Power Sources 278 (2015) 375–381.
[26] R. Gao, R. Tan, L. Han, Y. Zhao, Z. Wang, L. Yang, F. Pan, Nanofiber networks of $Na_3V_2(PO_4)_3$ as a cathode material for high performance all-solid-state sodium-ion batteries, J. Mater. Chem. A 5 (2017) 5273–5277.
[27] S. Chen, F. Feng, Y. Yin, H. Che, X.-Z. Liao, Z.-F. Ma, A solid polymer electrolyte based on star-like hyperbranched β-cyclodextrin for all-solid-state sodium batteries, J. Power Sources 399 (2018) 363–371.
[28] F. Colò, F. Bella, J.R. Nair, M. Destro, C. Gerbaldi, Cellulose-based novel hybrid polymer electrolytes for green and efficient Na-ion batteries, Electrochim. Acta 174 (2015) 185–190.
[29] X. Wang, X. Zhang, Y. Lu, Z. Yan, Z. Tao, D. Jia, J. Chen, Flexible and tailorable $Na-CO_2$ batteries based on an all-solid-state polymer electrolyte, ChemElectroChem 5 (2018) 3628–3632.
[30] L. Chen, Y. Li, S.-P. Li, L.-Z. Fan, C.-W. Nan, J.B. Goodenough, PEO/garnet composite electrolytes for solid-state lithium batteries: from "ceramic-in-polymer" to "polymer-in-ceramic", Nano. Energy 46 (2018) 176–184.
[31] T. Yang, J. Zheng, Q. Cheng, Y.-Y. Hu, C.K. Chan, Composite polymer electrolytes with $Li_7La_3Zr_2O_{12}$ garnet-type nanowires as ceramic fillers: mechanism of conductivity enhancement and role of doping and morphology, ACS Appl. Mater. Interfaces 9 (2017) 21773–21780.
[32] A. Sarnowska, I. Polska, L. Niedzicki, M. Marcinek, A. Zalewska, Properties of poly (vinylidene fluoride-co-hexafluoropropylene) gel electrolytes containing modified inorganic Al_2O_3 and TiO_2 filler, complexed with different lithium salts, Electrochim. Acta 57 (2011) 180–186.
[33] S. Bag, C. Zhou, P.J. Kim, V.G. Pol, V. Thangadurai, LiF modified stable flexible PVDF-garnet hybrid electrolyte for high performance all-solid-state Li–S batteries, Energy Storage Mater 24 (2020) 198–207.
[34] X. Cai, T. Lei, D. Sun, L. Lin, A critical analysis of the α, β and γ phases in poly (vinylidene fluoride) using FTIR, RSC Adv. 7 (2017) 15382–15389.
[35] P. Martins, A.C. Lopes, S. Lanceros-Mendez, Electroactive phases of poly (vinylidene fluoride): determination, processing and applications, Prog. Polym. Sci. 39 (2014) 683–706.
[36] F. Wang, L. Li, X. Yang, J. You, Y. Xu, H. Wang, Y. Ma, G. Gao, Influence of additives in a PVDF-based solid polymer electrolyte on conductivity and Li-ion battery performance, Sustain. Energy Fuels 2 (2018) 492–498.
[37] Y. Li, J.-Z. Xu, L. Zhu, H. Xu, M.-W. Pan, G.-J. Zhong, Z.-M. Li, Multiple stage crystallization of gamma phase poly(vinylidene fluoride) induced by ion-dipole interaction as revealed by time-resolved FTIR and two-dimensional correlation analysis, Polymer 55 (2014) 4765–4775.
[38] R.A. Sanders, R. Frech, M.A. Khan, Structural investigation of crystalline and solution phases in N,N,N',N'-Tetramethylethylenediamine (TMEDA) with lithium triflate ($LiCF_3SO_3$) and sodium triflate ($NaCF_3SO_3$), J. Phys. Chem. B 107 (2003) 8310–8315.
[39] S. Ramesh, T.F. Yuen, C.J. Shen, Conductivity and FTIR studies on PEO–LiX [X: $CF_3SO_3^-$, SO_4^{2-}] polymer electrolytes, Spectrochim. Acta A 69 (2008) 670–675.
[40] D.H. Johnston, D.F. Shriver, Vibrational study of the trifluoromethanesulfonate anion: unambiguous assignment of the asymmetric stretching modes, Inorg. Chem. 32 (1993) 1045–1047.
[41] C. Zhou, S. Bag, T. He, B. Lv, V. Thangadurai, A 20 °C operating high capacity solid-state Li-S battery with an engineered carbon support cathode structure, Appl. Mater. Today 19 (2020), 100585.
[42] S. Schantz, On the ion association at low salt concentrations in polymer electrolytes; a Raman study of $NaCF_3SO_3$ and $LiClO_4$ dissolved in poly(propylene oxide), J. Chem. Phys. 94 (1991) 6296–6306.
[43] S. Schantz, J. Sandahl, L. Börjesson, L.M. Torell, J.R. Stevens, Ion pairing in polymer electrolytes; A comparative Raman study of $NaCF_3SO_3$ complexed in poly (propylene-glycol) and dissolved in acetonitrile, Solid State Ionics 28–30 (1988) 1047–1053.
[44] P.N. Didwal, R. Verma, C.-W. Min, C.-J. Park, Synthesis of 3-dimensional interconnected porous $Na_3V_2(PO_4)_3$@C composite as a high-performance dual electrode for Na-ion batteries, J. Power Sources 413 (2019) 1–10.
[45] Y. Fang, J. Zhang, L. Xiao, X. Ai, Y. Cao, H. Yang, Phosphate framework electrode materials for sodium ion batteries, Adv. Sci. 4 (2017), 1600392.
[46] Z. Wu, S. Ji, T. Liu, Y. Duan, S. Xiao, Y. Lin, K. Xu, F. Pan, Aligned Li^+ tunnels in core–shell $Li(Ni_xMn_yCo_z)O_2$@$LiFePO_4$ enhances its high voltage cycling stability as Li-ion battery cathode, Nano Lett. 16 (2016) 6357–6363.
[47] X. Zhang, X. Rui, D. Chen, H. Tan, D. Yang, S. Huang, Y. Yu, $Na_3V_2(PO_4)_3$: an advanced cathode for sodium-ion batteries, Nanoscale 11 (2019) 2556–2576.
[48] B. Kumar, L.G. Scanlon, R.J. Spry, On the origin of conductivity enhancement in polymer-ceramic composite electrolytes, J. Power Sources 96 (2001) 337–342.
[49] D. Bresser, S. Lyonnard, C. Iojoiu, L. Picard, S. Passerini, Decoupling segmental relaxation and ionic conductivity for lithium-ion polymer electrolytes, Mol. Syst. Des. Eng. 4 (2019) 779–792.
[50] Z. Wang, B. Huang, S. Wang, R. Xue, X. Huang, L. Chen, Competition between the plasticizer and polymer on associating with Li + ions in polyacrylonitrile-based electrolytes, J. Electrochem. Soc. 144 (1997) 778–786.
[51] S.F. Mendes, C.M. Costa, C. Caparros, V. Sencadas, S. Lanceros-Méndez, Effect of filler size and concentration on the structure and properties of poly(vinylidene fluoride)/$BaTiO_3$ nanocomposites, J. Mater. Sci. 47 (2012) 1378–1388.
[52] C. Shen, J. Wang, Z. Tang, H. Wang, H. Lian, J. Zhang, C.-n. Cao, Physicochemical properties of poly(ethylene oxide)-based composite polymer electrolytes with a silane-modified mesoporous silica SBA-15, Electrochim. Acta 54 (2009) 3490–3494.
[53] G. Bieker, M. Winter, P. Bieker, Electrochemical in situ investigations of SEI and dendrite formation on the lithium metal anode, Phys. Chem. Chem. Phys. 17 (2015) 8670–8679.

[54] Z. Jian, Y. Sun, X. Ji, A new low-voltage plateau of $Na_3V_2(PO_4)_3$ as an anode for Na-ion batteries, Chem. Commun. 51 (2015) 6381–6383.
[55] Y. Zhang, H. Zhao, Y. Du, Symmetric full cells assembled by using self-supporting $Na_3V_2(PO_4)_3$ bipolar electrodes for superior sodium energy storage, J. Mater. Chem. A 4 (2016) 7155–7159.
[56] W. Wang, Q. Xu, H. Liu, Y. Wang, Y. Xia, A flexible symmetric sodium full cell constructed using the bipolar material $Na_3V_2(PO_4)_3$, J. Mater. Chem. A 5 (2017) 8440–8450.
[57] C.V. Manohar, T.C. Mendes, M. Kar, D. wang, C. Xiao, M. Forsyth, S. Mitra, D. R. MacFarlane, Ionic liquid electrolytes supporting high energy density in sodium-ion batteries based on sodium vanadium phosphate composites, Chem. Commun. 54 (2018) 3500–3503.
[58] Y. Huang, L. Zhao, L. Li, M. Xie, F. Wu, R. Chen, Electrolytes and electrolyte/electrode interfaces in sodium-ion batteries: from scientific research to practical application, Adv. Mater. 31 (2019), 1808393.
[59] D. Wang, N. Chen, M. Li, C. Wang, H. Ehrenberg, X. Bie, Y. Wei, G. Chen, F. Du, $Na_3V_2(PO_4)_3$/C composite as the intercalation-type anode material for sodium-ion batteries with superior rate capability and long-cycle life, J. Mater. Chem. A 3 (2015) 8636–8642.
[60] Z. Jian, L. Zhao, H. Pan, Y.-S. Hu, H. Li, W. Chen, L. Chen, Carbon coated $Na_3V_2(PO_4)_3$ as novel electrode material for sodium ion batteries, Electrochem. Commun. 14 (2012) 86–89.
[61] C. Xu, B. Sun, T. Gustafsson, K. Edström, D. Brandell, M. Hahlin, Interface layer formation in solid polymer electrolyte lithium batteries: an XPS study, J. Mater. Chem. A 2 (2014) 7256–7264.
[62] W. Duan, Z. Zhu, H. Li, Z. Hu, K. Zhang, F. Cheng, J. Chen, $Na_3V_2(PO_4)_3$@C core–shell nanocomposites for rechargeable sodium-ion batteries, J. Mater. Chem. A 2 (2014) 8668–8675.
[63] S.-J. Lim, D.-W. Han, D.-H. Nam, K.-S. Hong, J.-Y. Eom, W.-H. Ryu, H.-S. Kwon, Structural enhancement of $Na_3V_2(PO_4)_3$/C composite cathode materials by pillar ion doping for high power and long cycle life sodium-ion batteries, J. Mater. Chem. A 2 (2014) 19623–19632.
[64] S.Y. Lim, H. Kim, R.A. Shakoor, Y. Jung, J.W. Choi, Electrochemical and thermal properties of NASICON structured $Na_3V_2(PO_4)_3$ as a sodium rechargeable battery cathode: a combined experimental and theoretical study, J. Electrochem. Soc. 159 (2012) A1393–A1397.
[65] V. Aravindan, Y.-S. Lee, S. Madhavi, Best practices for mitigating irreversible capacity loss of negative electrodes in Li-ion batteries, Adv. Energy Mater. 7 (2017), 1602607.
[66] X. Liu, X. Jiang, F. Zhong, X. Feng, W. Chen, X. Ai, H. Yang, Y. Cao, High-safety symmetric sodium-ion batteries based on nonflammable phosphate electrolyte and double $Na_3V_2(PO_4)_3$ electrodes, ACS Appl. Mater. Interfaces 11 (2019) 27833–27838.
[67] X. Yao, Z. Zhu, Q. Li, X. Wang, X. Xu, J. Meng, W. Ren, X. Zhang, Y. Huang, L. Mai, 3.0 V high energy density symmetric sodium-ion battery: $Na_4V_2(PO_4)_3$||$Na_3V_2(PO_4)_3$, ACS Appl. Mater. Interfaces 10 (2018) 10022–10028.